Fast calculation of pulsed photoacoustic fields in fluids using *k*-space methods

B. T. Cox[a] and P. C. Beard
Department of Medical Physics and Bioengineering, University College London, Gower Street, London WC1E 6BT, United Kingdom

(Received 8 December 2004; revised 31 March 2005; accepted 31 March 2005)

Two related numerical models that calculate the time-dependent pressure field radiated by an arbitrary photoacoustic source in a fluid, such as that generated by the absorption of a short laser pulse, are presented. Frequency-wavenumber (*k*-space) implementations have been used to produce fast and accurate predictions. Model I calculates the field everywhere at any instant of time, and is useful for visualizing the three-dimensional evolution of the wave field. Model II calculates pressure time series for points on a straight line or plane and is therefore useful for simulating array measurements. By mapping the vertical wavenumber spectrum directly to frequency, this model can calculate time series up to 50 times faster than current numerical models of photoacoustic propagation. As the propagating and evanescent parts of the field are calculated separately, model II can be used to calculate far- and near-field radiation patterns. Also, it can readily be adapted to calculate the velocity potential and thus particle velocity and acoustic intensity vectors. Both models exploit the efficiency of the fast Fourier transform, and can include the frequency-dependent directional response of an acoustic detector straightforwardly. The models were verified by comparison with a known analytic solution and a slower, but well-understood, numerical model. [DOI: 10.1121/1.1920227]

PACS numbers: 43.35.Ud, 43.20.Px [YHB] Pages: 3616–3627

I. INTRODUCTION

There are several mechanisms by which electromagnetic radiation incident on a solid or fluid can generate acoustic waves, e.g., ablation, electrostriction, and thermoelastic expansion.[1] This paper is concerned with the prediction of the acoustic field generated in a fluid due to thermoelastic expansion following localized absorption of an electromagnetic pulse.

A number of papers present analytical solutions for the photoacoustic pressure under specific circumstances. In particular, Tam[1] quotes analytical solutions for the pressure for narrow and Gaussian laser beams in weakly absorbing fluids. Diebold *et al.* have presented many analytical solutions for the acoustic pressure caused by a variety of geometries of photoacoustic sources, including among others infinitely long Gaussian sources, point sources, and solid spheres.[2–6] All of these analytical solutions have the disadvantage that they are restricted to a particular case; the photoacoustic source must have a certain geometry. A time-domain numerical model of photoacoustic propagation that can include an arbitrary initial pressure distribution has been described in the literature[7–9] and is compared, in Sec. VI A, to the *k*-space models derived here. It is based on Poisson's integral solution to the wave equation[10] and provides an intuitive method useful for predicting the time evolution of the pressure at a point. For applications that require the pressure to be known at many points and small distances from the source it is considerably slower than the *k*-space models.[9]

Two models—model I and model II—that calculate the field generated by an arbitrarily shaped initial pressure distribution (or photoacoustic source) are presented in this paper. These propagation models fall into the category of wavenumber integration algorithms. Propagation models based on numerically solving a wavenumber integral are in widespread use in underwater acoustics and seismology.[11] This is mainly because these techniques lend themselves to the use of the fast Fourier transform (FFT) algorithm, and are therefore computationally efficient. Similar techniques have not previously been applied to the specific problem of the propagation of photoacoustic signals.

Model I uses an exact time propagator to calculate the acoustic field at all points on a grid for a single time following the absorption of an electromagnetic pulse. Unlike finite difference methods, in which the time step must be small to avoid instability, the acoustic field at any time may be predicted in one step without the need to calculate the field at intermediate times. With this model, the evolution of 3D fields through time can be visualized.

Model II, rather than calculating the pressure everywhere at a single time, calculates the pressure on a chosen line or plane for many times at once. It maps the pressure as a function of vertical spatial wavenumber to the pressure as a function of temporal frequency which results in a significant increase in speed over model I. For applications that do not require knowledge of the entire spatial field, e.g., for simulating the temporal signals detected by an array of sensors, this may be useful. The propagating and evanescent parts of the field are calculated separately in this model. As it is often convenient to neglect the evanescent part of the field, this model can show under which circumstances this is reasonable. In addition, model II may be used to generate near- and

[a]Electronic mail: bencox@medphys.ucl.ac.uk

 0001-4966/2005/117(6)/3616/12/$22.50

far-field single-frequency or broadband radiation patterns of photoacoustic sources, and simply adapted to calculate velocity potential, and thus particle velocity and acoustic intensity vectors.

These two *k*-space models allow photoacoustic fields to be calculated as much as 50 times faster than previous numerical techniques, with high accuracy as determined by comparisons with analytical results. They are more general than known analytical solutions, which usually include restrictive assumptions about the photoacoustic source geometry, and more efficient than current time-domain models. Both models can include the effect of an arbitrary, complex, frequency-dependent, directional detector response on the measured pressure, thus simulating not just the photoacoustic wave propagation but also its measurement. This is crucial for accurate simulations of measurements made by an array of detectors, for instance, when studying acoustic inverse problems such as photoacoustic imaging.[12–15] Indeed, photoacoustic imaging is one of the growing number of applications of photoacoustics to which these propagation models are applicable.

II. PHOTOACOUSTIC WAVE EQUATION

If a region of a fluid is heated, through the absorption of a laser pulse, a sound wave will be generated. Consider a stationary fluid with isotropic acoustic properties. Under conditions whereby the sound generation mechanism is thermoelastic, and terms containing the viscosity and thermal conductivity are negligible (thermal confinement),[16] the acoustic pressure, in the linear approximation, obeys the wave equation

$$\nabla^2 p - \frac{1}{c^2}\frac{\partial^2 p}{\partial t^2} = \frac{-\beta}{C_p}\frac{\partial \mathcal{H}}{\partial t}, \tag{1}$$

where c is the sound speed, β is the volume thermal expansivity, C_p is the specific heat capacity, and $\mathcal{H}$ is the heat energy per unit volume and per unit time deposited in the fluid; p and $\mathcal{H}$ will depend, in general, on the position $\mathbf{x}=(x,y,z)$ and time t.

The heating is caused by the absorption of light. If the light fluence rate at a point in the fluid is $F(\mathbf{x},t)$ and the absorption distribution $\mu_a(\mathbf{x})$, then the heating function can be written as $\mathcal{H}(\mathbf{x},t)=\mu_a(\mathbf{x})F(\mathbf{x},t)$. Note that the fluence rate F will in general depend on the absorption $\mu_a(\mathbf{x})$ and scattering; hence, the heating function is nonlinearly related to the absorption distribution.

A. Instantaneous heating

When the laser pulse is short, so the density of the fluid has no time to change, it may be modeled as a δ function. This is satisfied if the duration of the laser pulse t_p is much shorter than the time it takes sound to travel across the heated region, a condition known as stress confinement.[16] In this case, the heating function can be written as

$$\mathcal{H}(\mathbf{x},t)=H(\mathbf{x})\,\delta(t), \tag{2}$$

where $H(\mathbf{x})$ is the heat deposited in the fluid per unit volume.[17] In this idealized case, all of the optical energy will be absorbed before the fluid density has time to change. Under this isochoric condition, the increase in the temperature T' of the heated fluid region is related to the absorbed energy H by C_v, the constant volume specific heat capacity, and ρ, the ambient density: $T'=H/(\rho C_v)$. The thermodynamic relation $\rho'=\rho\kappa_T p'-\beta\rho T'$, where ρ' and p' are small changes in density and pressure, respectively, holds true for constant isothermal compressibility κ_T and volume thermal expansivity β. If there is no change in the density, so $\rho'=0$, then $p'=(\beta/\kappa_T)T'$. Using the expression for T' above and noting that $\kappa_T=\gamma/\rho c^2$, where γ is the specific heat ratio, the increase in pressure due to the absorption of the laser pulse, from here on called the initial pressure distribution $p_0(\mathbf{x})$, may be written

$$p_0(\mathbf{x})=\left(\frac{\beta c^2}{C_p}\right)H(\mathbf{x})=\Gamma H(\mathbf{x}), \tag{3}$$

where Γ is the Grüneisen coefficient, a dimensionless constant that represents the efficiency of the conversion of heat to pressure. For water at room temperature $\Gamma\approx 0.11$.

With the heating function given by Eq. (2), the solution to Eq. (1), in the absence of acoustic boundaries, can be written in terms of the Green's function as

$$p(\mathbf{x},t)=\frac{\beta}{C_p}\int_0^\infty\int_V G(\mathbf{x},t;\mathbf{x}',t')H(\mathbf{x}')\,\delta'(t')\,\mathrm{d}\mathbf{x}'\,\mathrm{d}t', \tag{4}$$

where δ' represents the derivative of the delta function, and the free-space Green's function G is a solution to

$$\nabla^2 G-\frac{1}{c^2}\frac{\partial^2 G}{\partial t^2}=-\delta(\mathbf{x}-\mathbf{x}')\,\delta(t-t'), \tag{5}$$

and is often written as

$$G(\mathbf{x},t;\mathbf{x}',t')=\frac{\delta[|\mathbf{x}-\mathbf{x}'|-c(t-t')]}{4\pi|\mathbf{x}-\mathbf{x}'|}, \tag{6}$$

representing a spherical wave traveling outward from $\mathbf{x}'$. Using the property of the δ function deriviative $\int\delta'(t-t_0)f(t)\mathrm{d}t=-f'(t_0)$, and noting that $\delta G/\partial t'=-\partial G/\partial t$, Eq. (4) becomes

$$p(\mathbf{x},t)=\frac{\beta}{C_p}\int_V H(\mathbf{x}')\frac{\partial G}{\partial t}(\mathbf{x},t;\mathbf{x}',t')\mathrm{d}\mathbf{x}'. \tag{7}$$

With Eq. (3), this gives the pressure at time t as

$$p(\mathbf{x},t)=\frac{1}{c^2}\int_V p_0(\mathbf{x}')\frac{\partial G}{\partial t}(\mathbf{x},t;\mathbf{x}',t')\mathrm{d}\mathbf{x}'. \tag{8}$$

B. Initial value problem

It is instructive to see that, whereas in the previous section the wave equation included a source term, in the case of instantaneous heating this problem can be recast as an initial value problem with no explicit source term but with the distribution of pressure at the instant of the laser pulse, $p_0(\mathbf{x})$, taken as given. This makes the two initial conditions required for a unique solution explicit. We solve the homogeneous wave equation [Eq. (1) with no source term] with the two initial conditions

$$p|_{t=0}=p_0(\mathbf{x}), \quad \left.\frac{\partial p}{\partial t}\right|_{t=0}=0. \tag{9}$$

The first condition defines the acoustic pressure distribution at $t=0$, the instant of the pulse. The second initial condition is equivalent to assuming the particle velocity $\mathbf{v}(\mathbf{x})$ is initially zero everywhere. In the absence of acoustic boundaries the solution to this initial value problem may be written in terms of the Green's function, G, and the initial conditions as[18]

$$p(\mathbf{x},t)=\frac{1}{c^2}\int_V\left[G\frac{\partial p}{\partial t'}-p\frac{\partial G}{\partial t'}\right]_{t'=0}\mathrm{d}\mathbf{x}'. \tag{10}$$

Using Eq. (9), we see that this solution is identical to Eq. (8).

C. Green's function in *k* space

In this paper we are interested in k-space methods for calculating the pressure field. To find an expression for the Green's function in terms of frequency and wavenumbers, we take a 4D Fourier transform of Eq. (5) with respect to t and $\mathbf{x}$

$$-k^2G(\omega,\mathbf{k})+\frac{\omega^2}{c^2}G(\omega,\mathbf{k})=-\mathrm{e}^{-i\mathbf{k}\cdot\mathbf{x}'}\mathrm{e}^{i\omega t'}. \tag{11}$$

The free-space Green's function G may then be written in terms of the wavenumber vector $\mathbf{k}=(k_x,k_y,k_z)$ and frequency ω as a fourfold inverse Fourier transform

$$G(\mathbf{x},t;\mathbf{x}',t')=\frac{1}{(2\pi)^4}\int\int\frac{\mathrm{e}^{i\mathbf{k}\cdot(\mathbf{x}-\mathbf{x}')}\mathrm{e}^{-i\omega(t-t')}}{k^2-(\omega/c)^2}\mathrm{d}\omega\,\mathrm{d}\mathbf{k}, \tag{12}$$

where $k=|\mathbf{k}|$. In Eq. (6) the Green's function is written as a spherical wave; in Eq. (12) this spherical wave is expressed as a sum of plane waves with direction given by $\mathbf{k}$ and frequency ω.

The two algorithms described below for calculating $p(\mathbf{x},t)$ from the initial pressure $p_0(\mathbf{x})$ are derived by analytically evaluating, in the first case, the ω integral in Eq. (12) and, in the second case, the integral over the vertical wavenumber k_z. The first results in a solution for the whole field at one instant in time, and the second in a method that calculates a pressure time series at all points on a line or plane. In both cases the singularity in the integrand in Eq. (12) at $\omega=ck$ is dealt with using contour integration.

III. MODEL I: THE WHOLE FIELD FOR ONE TIME

As noted above, the integrand in Eq. (12) is singular when $\omega=ck$. However, we can evaluate the integral using Cauchy's residue theorem. First, the difference of the two squared terms in the denominator is rewritten so the ω integral in Eq. (12), with t' set to zero, becomes

$$\int\frac{\mathrm{e}^{i\mathbf{k}\cdot(\mathbf{x}-\mathbf{x}')}\mathrm{e}^{-i\omega t}}{(k-\omega/c)(k+\omega/c)}\mathrm{d}\omega, \tag{13}$$

from which it is clear that there are two simple poles on the real ω axis at $\pm ck$. This can be solved using Cauchy's residue theorem[18] to give Eq. (12), for $t>0$, as

$$G(\mathbf{x},t;\mathbf{x}')=\frac{c}{(2\pi)^3}\int\frac{\sin(ckt)}{k}\mathrm{e}^{i\mathbf{k}\cdot(\mathbf{x}-\mathbf{x}')}\mathrm{d}\mathbf{k}. \tag{14}$$

The Green's function is now a sum of plane waves with different spatial frequencies multiplied by a time propagator. The time derivative of G is

$$\frac{\partial G}{\partial t}=\frac{c^2}{(2\pi)^3}\int\cos(ckt)\mathrm{e}^{i\mathbf{k}\cdot(\mathbf{x}-\mathbf{x}')}\mathrm{d}\mathbf{k}. \tag{15}$$

Substituting this into Eq. (8) gives a solution for the pressure in a free-field given an initial pressure distribution

$$p(\mathbf{x},t)=\frac{1}{(2\pi)^3}\int\int p_0(\mathbf{x}')\cos(ckt)\mathrm{e}^{i\mathbf{k}\cdot(\mathbf{x}-\mathbf{x}')}\mathrm{d}\mathbf{k}\,\mathrm{d}\mathbf{x}'. \tag{16}$$

Changing the order of the integration gives a two-stage method for calculating $p(\mathbf{x},t)$ at a given time t. First, the 3D spatial Fourier transform of the initial pressure distribution is taken (here the primes have been dropped)

$$p_0(\mathbf{k})=\int p_0(\mathbf{x})\mathrm{e}^{-i\mathbf{k}\cdot\mathbf{x}}\mathrm{d}\mathbf{x}, \tag{17}$$

and second, the pressure at time t is calculated using

$$p(\mathbf{x},t)=\frac{1}{(2\pi)^3}\int p_0(\mathbf{k})\cos(ckt)\mathrm{e}^{i\mathbf{k}\cdot\mathbf{x}}\mathrm{d}\mathbf{k}. \tag{18}$$

So, if the heating function $H(\mathbf{x})$ is known, $p_0(\mathbf{x})$ is known from Eq. (3), and the acoustic pressure at all positions and subsequent times can be calculated using Eqs. (17) and (18). To calculate the field at any time t thus requires just two 3D FFTs and one multiplication. Because the changes of p over time are calculated using the exact propagator $\cos(ckt)$ and not from an approximation, it is not necessary to calculate the field at intermediate times, as it is with finite difference methods, for instance. In practice the pressure is calculated on a grid of points, in which case the grid spacing must meet the usual Nyquist criterion to avoid aliasing in the spatial domain; it must be less than half the minimum wavelength. This first k-space method is similar to that proposed by Healey *et al.*[19] As the field is calculated everywhere in one step, it is a useful method for visualizing the field from a source at a particular time. Illustrations of this are given in Sec. VII A.

IV. MODEL II: TIME SERIES

Model I calculates the spatial distribution of the field everywhere for one instant of time. This can be slow if the pressure at just a single point or a few points is required as a function of time. Model II calculates a pressure time series at points on a line or plane. For applications in which a time series is required at only a few points in the field, or for simulating the signals measured by an array of detectors, this method may be much faster than model I.

In the above section the ω integral in Eq. (12) was calculated analytically. This resulted in a 3D Fourier transform in spatial wavenumbers to calculate the pressure field at one time. To arrive at a method that calculates the pressure at many times (a time series) in a single step, we need to leave

the Fourier transform with respect to ω in the expression. To this end we consider analytically evaluating the integral over k_z, the vertical component of the wavenumber vector $\mathbf{k}$, as a means of removing the singularities in Eq. (12). The simple poles at $k_z=\pm\zeta$ are clear if we rewrite this integral as

$$\int \frac{e^{i\mathbf{k}\cdot(\mathbf{x}-\mathbf{x}')}e^{-i\omega t}}{(k_z-\zeta)(k_z+\zeta)}\,dk_z, \tag{19}$$

where we have chosen

$$\begin{aligned}\zeta&=\mathrm{sgn}(\omega)\sqrt{(\omega/c)^2-k_r^2} \quad \text{for } |\omega/c|\geqslant k_r,\\ \zeta&=+i\sqrt{k_r^2-(\omega/c)^2} \quad \text{for } |\omega/c|<k_r.\end{aligned} \tag{20}$$

Here, $k_r=\sqrt{k_x^2+k_y^2}$ and $\mathrm{sgn}(\omega)=+1$ for $\omega\geqslant 0$ and -1 for $\omega<0$. As before, Eq. (19) can be solved using Cauchy's residue theorem[20] to give the Green's function for $t>0$ as

$$G(\mathbf{x},t;\mathbf{x}')=\frac{i\pi}{(2\pi)^4}\int\int\int\left(\frac{1}{\zeta}\right)\times e^{i[k_x(x-x')+k_y(y-y')+\zeta|z-z'|-\omega t]}\,d\omega\,dk_x\,dk_y. \tag{21}$$

Compare the Green's function here, written as a sum of plane waves in x, y, and t, with the formulation in Eq. (12) as a sum of plane waves in $\mathbf{x}$. The time derivative of G is

$$\frac{\partial G}{\partial t}=\frac{\pi}{(2\pi)^4}\int\int\int\left(\frac{\omega}{\zeta}\right)\times e^{i[k_x(x-x')+k_y(y-y')+\zeta|z-z'|-\omega t]}\,d\omega\,dk_x\,dk_y, \tag{22}$$

and, using Eq. (8), the pressure $p(\mathbf{x},t)$ may be written

$$p(\mathbf{x},t)=\frac{\pi}{(2\pi)^4c^2}\int_V\int\int\int\left(\frac{\omega}{\zeta}\right)p_0(\mathbf{x}')\times e^{i[k_x(x-x')+k_y(y-y')+\zeta|z-z'|-\omega t]}\,d\omega\,dk_x\,dk_y\,d\mathbf{x}'. \tag{23}$$

Because of the two definitions of ζ, Eq. (20), it is convenient to consider the pressure field as a sum of propagating and evanescent components

$$p(\mathbf{x},t)=p_{\mathrm{prop}}(\mathbf{x},t)+p_{\mathrm{evan}}(\mathbf{x},t). \tag{24}$$

These are considered separately below.

A. Propagating (radiating) part of the field

In Eq. (23) ζ is really just shorthand for $\mathrm{sgn}(\omega)\sqrt{(\omega/c)^2-k_r^2}$ or $+i\sqrt{k_r^2-(\omega/c)^2}$, depending on whether $|\omega/c|\geqslant k_r$ or $<k_r$ [see Eqs. (20)]. ζ is real when $|\omega/c|\geqslant k_r$. This part of the solution, p_{prop}, consists of plane waves that propagate away from the source region and eventually form the acoustic far field. For this propagating, or radiating, part of the acoustic field, the integral over ω in Eq. (23) may be rearranged to give

$$\begin{aligned}&\int_{|\omega|\geqslant ck_r}\left|\frac{\omega}{\zeta}\right|e^{i\zeta|z-z'|}e^{-i\omega t}\,d\omega\\ &=\int_{ck_r}^{\infty}\left(\frac{\omega}{\zeta}\right)\{e^{i\zeta|z-z'|}e^{-i\omega t}+e^{-i\zeta|z-z'|}e^{i\omega t}\}d\omega\\ &=2\Re\left\{\int_{ck_r}^{\infty}\left(\frac{\omega}{\zeta}\right)e^{i\zeta|z-z'|}e^{-i\omega t}\,d\omega\right\},\end{aligned} \tag{25}$$

where $\Re$ indicates the real part. Equation (23) calculates the pressure on the z plane. We can set $z=0$ without loss of generality. In this case the propagating part of the field may be written as

$$p_{\mathrm{prop}}(x,y,t)=\frac{1}{(2\pi)^3c^2}\Re\left\{\int\int\int\left(\frac{\omega}{\zeta}\right)p_0(k_x,k_y,\omega)\times e^{i(k_xx+k_yy-\omega t)}\,dk_x\,dk_y\,d\omega\right\}, \tag{26}$$

where the ω integral is from ck_r to ∞ and $p_0(k_x,k_y,\omega)$ is interpolated from $p_0(k_x,k_y,\zeta)$, below, using Eq. (20).

$$p_0(k_x,k_y,\zeta)=\int\int\int p_0(\mathbf{x}')e^{-i(k_xx'+k_yy'-\zeta|z'|)}\,d\mathbf{x}'. \tag{27}$$

This interpolation from ζ to ω, vertical wavenumber to temporal frequency, effectively maps depth information in $p_0(z)$ to time information in $p(t)$. Indeed, in the 1D case where p_0 varies only with z, the temporal signal $p(t)$ has the same shape as the depth function $p(t)\propto p_0(t=z/c)$.[4] The complex exponential Fourier kernels in Eqs. (26) and (27) mean that most of the computations can be performed efficiently using FFTs.

In Sec. IV B we see that the evanescent part of the field can be written as a sine transform in ω. It is interesting that the propagating part, Eq. (26), can be written as a cosine transform in ω if

$$\Im\left\{\int\int p_0(k_x,k_y,\omega)e^{i(k_xx+k_yy)}\,dk_x\,dk_y\right\}=0, \tag{28}$$

where $\Im$ indicates the imaginary part. This condition requires both $\Im\{p_0(k_x,k_y,\zeta)\}$ to be odd in k_x and k_y and independent of ζ, and $\Re\{p_0(k_x,k_y,\zeta)\}$ to be even in k_x, k_y. Nothing, so far, has been assumed about $p(t)$ for $t<0$. As we are only interested in $p(t)$ for $t\geqslant 0$ we can choose $p(t)$ for $t<0$ to be any function. We choose to make $p(t)$ even, $p(t)=p(-t)$. As pressure is a real quantity, if $p(t)$ is even then its Fourier transform must be a real, even, function of frequency ω. As $p_0(\mathbf{x}')$ is real this can be achieved by removing the imaginary part of $\exp(i\zeta|z|)$ in Eq. (27) to get

$$p_0(k_x,k_y,\zeta)=\int\int\int p_0(\mathbf{x}')e^{-i(k_xx'+k_yy')}\cos(\zeta|z'|)\,d\mathbf{x}'. \tag{29}$$

If $p_0(\mathbf{x}')$ is symmetrical about $z'=0$ this may be written as a Fourier transform, like Eq. (17), except with $\mathbf{k}$ replaced with (k_x,k_y,ζ). [If $p_0(\mathbf{x}')$ is not symmetrical about $z'=0$ we can make it so, by using $1/2[p_0(x',y',z')+p_0(x',y',-z')]$ as the initial pressure. This will have no effect on the

pressure predicted on $z=0$ and does not require that $p_0(\mathbf{x}')=0$ for $z<0$, i.e., the initial pressure distribution is not restricted to one side of the measurement surface.]

The condition in Eq. (28) is now satisfied and Eq. (26) becomes a cosine transform

$$p_{\text{prop}}(x,y,t)=\frac{1}{(2\pi)^3 c^2}\int\int\int\left(\frac{\omega}{\zeta}\right)p_0(k_x,k_y,\omega)\times e^{i(k_x x+k_y y)}\cos(\omega t)\,dk_x\,dk_y\,d\omega. \quad (30)$$

An advantage of writing the propagating part as a cosine transform is that by inverting the transforms we arrive at a method of estimating $p_0(\mathbf{x})$ from measurements of $p(x,y,t)$ on the $z=0$ plane. This photoacoustic imaging method has been described by Köstli *et al.*[21] It can be used to estimate the initial pressure distribution from time series measurements of the acoustic field along a line or plane. However, this method ignores the evanescent component. An advantage, therefore, of having a forward model that computes the propagating and evanescent parts separately is that we can study under what conditions the evanescent component of the field is indeed negligible and this imaging algorithm gives accurate results.

B. Evanescent part of the field

ζ is imaginary when $|\omega/c|<k_r$. This second part of the solution from Eq. (24), p_{evan}, consists of evanescent plane waves that decay exponentially with z. (They are sometimes called inhomogeneous waves as they decay with z but not with x and y.) These waves do not contribute to the field beyond a few wavelengths of the source. They must, however, be included when calculating the acoustic pressure close to the source region. In this case the integral over ω in Eq. (23) can be rearranged to

$$\int_{|\omega|<ck_r}\left(\frac{\omega}{\zeta}\right)e^{i\zeta|z-z'|}e^{-i\omega t}\,d\omega = -2i\int_0^{ck_r}\left(\frac{\omega}{\zeta}\right)e^{i\zeta|z-z'|}\sin(\omega t)\,d\omega. \quad (31)$$

If, as above, we set $z=0$, then the evanescent part of the field can be written

$$p_{\text{evan}}(x,y,t)=\frac{-i}{(2\pi)^3 c^2}\int\int\int\left(\frac{\omega}{\zeta}\right)p_0(k_x,k_y,\omega)\times e^{i(k_x x+k_y y)}\sin(\omega t)\,dk_x\,dk_y\,d\omega, \quad (32)$$

where the ω integral is from 0 to ck_r. By remembering that ζ is purely imaginary for evanescent waves, this may be written, for comparison with Eq. (26), as

$$p_{\text{evan}}(x,y,t)=\frac{1}{(2\pi)^3 c^2}\Re\left\{\int\int\int\left(\frac{\omega}{\zeta}\right)p_0(k_x,k_y,\omega)\times e^{i(k_x x+k_y y-\omega t)}\,dk_x\,dk_y\,d\omega\right\}. \quad (33)$$

[Note that in this equation the ω integral is taken from 0 to ck_r, whereas in Eq. (26) it is from ck_r to ∞.] As for the propagating part of the field, $p_0(k_x,k_y,\omega)$ is interpolated from $p_0(k_x,k_y,\zeta)$, which is given by Eq. (27). However, here $p_0(k_x,k_y,\zeta)$ is required at imaginary values of ζ from 0 to ik_r in order to interpolate to $p_0(k_x,k_y,\omega)$ for $0\leqslant\omega<ck_r$ using Eq. (20). This means that, because ζ is imaginary, Eq. (27) is no longer a Fourier transform in z', as it is for the propagating part, but instead contains an $\exp(-|\zeta z|)$ term.

$$p_0(k_x,k_y,\zeta)=\int\int\int p_0(\mathbf{x}')e^{-i(k_x x'+k_y y')}e^{-|\zeta z'|}\,d\mathbf{x}'. \quad (34)$$

As the decaying exponential term cannot be evaluated with an FFT, it is more time consuming to calculate the evanescent part and so it is an advantage in terms of speed when this part of the field can be neglected, e.g., in the far field.

C. Including a reflecting plane boundary

In some circumstances it is convenient to include a reflection from a plane boundary in the initial pressure distribution by using an image of $p_0(\mathbf{x})$. If we add a perfectly reflecting acoustic boundary at z_0, with reflection coefficient V, then the initial pressure becomes $p_0(x,y,z)+Vp_0(x,y,2z_0-z)$. Note there is a subtlety with the use of a reflecting boundary. The bounding material must be modeled as a fluid, and not a solid, in order to avoid a pole in V in k space corresponding to an interface wave which occurs when both shear and compressional waves are allowed. The singularity causes aliasing problems due to undersampling; see Sec. V B.

D. Including an arbitrary detector response

To predict the pressure measured by a sensor, rather than the pressure at a single point, it is necessary to take into account the averaging effect due to its finite size. A wavenumber model of a planar detector response, $\mathcal{D}$, may be included straightforwardly by multiplying $p_0(k_x,k_y,\omega)$ in Eq. (30) by the detector response $\mathcal{D}(k_x,k_y,\omega)$. [In a similar way, the detector response can be included in model I by multiplying $p_0(\mathbf{k})$ in Eq. (18) by $\mathcal{D}(\mathbf{k})$.] As a simple example, a detector that averages the pressure over a small circle of radius a in the (x,y) plane has a directional response $\mathcal{D}(k_x,k_y)\equiv\mathcal{D}(k_r)\propto J_1(k_r a)/(k_r a)$. For a (multilayered) planar transducer[22,23] $\mathcal{D}$ can often be calculated using a wavenumber model.[24]

If $\mathcal{D}$ or V are complex, then it is necessary to use Eq. (26) to calculate the propagating part of the pressure and not Eq. (30), which requires condition Eq. (28) to hold. As there is no disadvantage in using Eq. (26) over Eq. (30), this presents no limitation in practice.

E. Implementation

In practice, this propagation model will be implemented with distances and wavenumbers discretized. In this case care must be taken over the sampling of the oscillating, and possibly ''spiky,'' integrands. In addition, there is a singularity at $\zeta=0$ in Eqs. (30) and (32). Consider the numerical integration of these equations. The singularity means that

however finely it is sampled it will always be undersampled; the samples can never properly reproduce the infinite peak. As undersampling in the Fourier domain appears as aliasing in the space domain, calculating the pressure field with Eq. (30) using FFTs, just as it stands without treating the singularity, will give inaccurate results. If the peak in the integrand can be smoothed to prevent the undersampling without sacrificing accuracy, then it will be possible to keep the solution in the form of a 3D FFT. One possible way to achieve this might be to shift the path of one of the integrals, say the k_x integral, off the real k_x axis into the complex plane, so the integral is over a contour from $-\infty+i\epsilon<k_x<\infty+i\epsilon$ instead of $-\infty<k_x<\infty$, thus moving away from the pole.[11] This approach is the subject of current research. The approach taken here is to remove the singularity with a change of variables. This is discussed in detail for the cylindrically symmetric case of model II in Sec. V. The disadvantage of this method is that the integral is no longer in the form of a 3D Fourier transform, but a 2D FFT and a sum. The sampling issue is also considered, for the cylindrically symmetric model, in Sec. V B.

V. MODEL II FOR A CYLINDRICALLY SYMMETRIC HEATING FUNCTION

It may be practical to reduce the 3D model to two dimensions when implementing these models. If a heating function $H(x,y,z)$ (heat deposited per unit volume) varies much less in one dimension, y say, than in the other two, it may be reasonable to assume it is constant with respect to y and calculate the pressure as a function of just x and z: $p(x,z,t)$. This 2D case can be straightforwardly implemented using the equations for the 3D case by setting $y=0$.

In many cases of practical interest the heating function H, and hence the initial pressure distribution, is cylindrically symmetric, with no dependence on angle. The output of a laser, or fiber-coupled laser, for instance, often exhibits cylindrical symmetry. In this case two of the Fourier transforms become a Hankel transform over a radial coordinate. This section describes the implementation of model II in this case, discussing algebraic forms of the heating function and the sampling requirements for the numerical calculations.

If $H(\mathbf{x}')=H(r',z')$ we can write the Fourier transforms over x' and y' in Eq. (27) or (34) as a Hankel transform over $r'=\sqrt{x^2+y^2}$. Dropping the primes, we have, for the propagating part

$$p_0(k_r,\zeta)=(2\pi)\int_{-\infty}^{\infty}\int_0^{\infty}p_0(r,z)e^{i\zeta|z|}J_0(k_r r)r\,dr\,dz, \tag{35}$$

and, for the evanescent part

$$p_0(k_r,\zeta)=(2\pi)\int_{-\infty}^{\infty}\int_0^{\infty}p_0(r,z)e^{-|\zeta z|}J_0(k_r r)r\,dr\,dz. \tag{36}$$

As before, $p_0(k_r,\omega)$ is interpolated from $p_0(k_r,\zeta)$ using Eqs. (20). To include the effect of a detector response $\mathcal{D}(k_r,\omega)$, we use $p_0(k_r,\omega)\mathcal{D}(k_r,\omega)$ in place of p_0, as in Sec. IV D. The integrals over k_x and k_y in Eqs. (30) and (32) also become Hankel transforms in $k_r=\sqrt{k_x^2+k_y^2}$ and the singularity when $\zeta=0$ is removed by making a change of variable. Changing from k_r to ϕ such that $k_r=(\omega/c)\cos\phi$ gives

$$p_{\text{prop}}(r,\omega)=A\omega^2\int_0^{\pi/2}p_0(\phi,\omega)\times J_0(r\omega\cos\phi/c)\cos\phi\,d\phi, \tag{37}$$

and, for the evanescent part, $k_r=(\omega/c)\cosh\phi$ gives

$$p_{\text{evan}}(r,\omega)=-A\omega^2\int_0^{\infty}p_0(\phi,\omega)\times J_0(r\omega\cosh\phi/c)\cosh\phi\,d\phi, \tag{38}$$

where $A=1/(2\pi c^3)$. The real part of the one-sided Fourier transform of $p_{\text{prop}}(r,\omega)$ gives the time series $p_{\text{prop}}(r,z=0,t)$. (If p_{prop} is assumed symmetrical about $t=0$ then this reduces to a one-sided cosine transform.) A sine transform of the evanescent part $p_{\text{evan}}(r,\omega)$ gives $p_{\text{evan}}(r,z=0,t)$. This derivation is for a detector at $z=0$, although it may be straightforwardly generalized to other detector depths.

A. Cylindrically symmetric heating functions

In the most general case the heating function $H(r,z)$, and hence initial pressure $p_0(r,z)=\Gamma H(r,z)$, will be given as values on a grid. In this case numerical Fourier and Hankel transforms[25,26] may be used to calculate $p_0(k_r,\zeta)$ from Eqs. (35) and (36). It may be, however, that $H(r,z)$ can be approximated by an algebraic expression. In such cases it may be possible to calculate the Hankel and Fourier transforms of $p_0(r,z)$ analytically. For instance, H may be approximated by a polynomial and the Hankel transform and Fourier transforms calculated by hand or looked up in a table. This can result in a significant increase in speed and accuracy as it removes the need for numerical Hankel transforms and interpolations.

Consider the example of a short laser pulse with a known beam profile, incident on the surface of a nonscattering fluid absorber (Fig. 1). The heating function may be separated into z- and r-dependent parts

$$H(r,z)=\mu_a E_0\hat{H}_r(r)\hat{H}_z(z), \tag{39}$$

where μ_a is the optical absorption coefficient, E_0 is the energy contained in a single pulse, and $\hat{H}_z(z)$ and $\hat{H}_r(r)$ are appropriately normalized shape functions that give the z and r dependence of the initial pressure distribution. If there is an acoustic impedance mismatch at the surface of the fluid that will cause reflections, then an image source may be included in $\hat{H}_z$ and, in this way, the acoustic effects of the boundary may be accounted for, as discussed in Sec. IV C. Examples of algebraic heating functions that might be useful in this scenario are given below. The depth dependence and radial dependence (beam profile) are treated separately.

1. Algebraic depth functions

For a pure absorber a distance z_0 above the measurement plane, the part of the heating function that depends on depth will be, according to Beer's law[27]

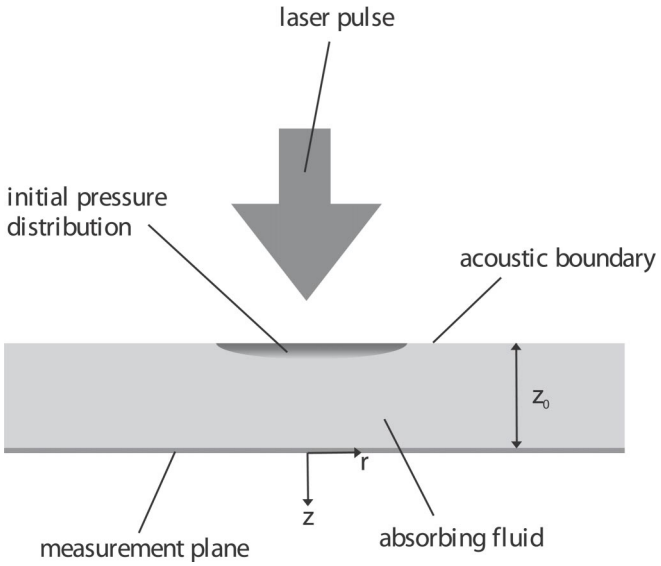

FIG. 1. An example of a cylindrically symmetric heating function, as described in Sec. V A.

$$\hat{H}_z(z) = \exp(-\mu_a(z+z_0)) \quad \text{for } z \geqslant -z_0$$
$$= 0 \quad \text{for } z < -z_0. \tag{40}$$

This assumes there is no acoustic impedance mismatch at the surface of the absorber. If, however, there is a transparent material with different acoustic properties above the absorber then there will be an acoustic reflection there. In general the reflection coefficient will depend on the horizontal wavenumber and frequency, $V(k_r, \omega)$. In this more general situation the depth function becomes

$$\hat{H}_z(z) = \exp(-\mu_a(z+z_0)) \quad \text{for } z \geqslant -z_0$$
$$= V \exp(\mu_a(z+z_0)) \quad \text{for } z < -z_0. \tag{41}$$

Substituting $\hat{H}_z(z)$ into the z integral (Fourier transform) in Eq. (35) we get

$$\hat{H}_z(\zeta) = \left(\frac{V e^{i\zeta z_0} + e^{-\mu_a z_0}}{\mu_a - i\zeta}\right) + \left(\frac{e^{i\zeta z_0} - e^{-\mu_a z_0}}{\mu_a + i\zeta}\right). \tag{42}$$

[If we use a cosine transform to transform the propagating part to the time domain, then we must use only the real part of Eq. (42). This is equivalent to calculating the cosine transform of $\hat{H}_z(z)$ using Eq. (29), instead of the full Fourier transform, and implicitly assumes $p(t) = p(-t)$.]

2. Algebraic beam profiles

For a laser beam with a Gaussian profile, the radial part of the heating function may be written as

$$\hat{H}_r(r) = e^{-(r/\sigma)^2}. \tag{43}$$

The Hankel transform of this is[28]

$$\hat{H}_r(k_r) = \left(\frac{\sigma^2}{2}\right) e^{-(k_r\sigma/2)^2}. \tag{44}$$

For a top hat beam profile:

$$\hat{H}_r(r) = 1 \quad \text{for } r \leqslant \sigma$$
$$0 \quad \text{for } r > \sigma, \tag{45}$$

which has a Hankel transform

$$\hat{H}_r(k_r) = \sigma \frac{J_1(k_r\sigma)}{k_r}. \tag{46}$$

B. Sampling

When Eqs. (37) and (38) are implemented the integrals will be approximated by summations. For this approximation to be accurate the oscillating integrands must be sampled more than once per oscillation. If the heating function is given by Eqs. (42) and (46), and if two adjacent samples of ϕ are separated by $\Delta\phi$, then the sampling criterion for Eq. (37) is

$$\Delta\phi < \frac{2\pi}{(r+z+\sigma)k}, \tag{47}$$

and for Eq. (38) is

$$\Delta\phi < \frac{2\pi}{k(r\sinh\phi_{\max} + z\cosh\phi_{\max} + \sigma\sinh\phi_{\max})}, \tag{48}$$

where $\phi_{\max}$ is the practical upper limit of the integral. If $\phi_{\max}$ is chosen, fairly arbitrarily, to be $\pi/2$, then this criterion is more stringent than that for the propagating part, as $\sinh(\pi/2) \approx 2.3$ and $\cosh(\pi/2) \approx 2.5$. This choice of $\phi_{\max}$ will be sufficiently high so long as $\hat{H}_r(k_r)$ is negligible above $k_r = (\omega/c)\cosh(\pi/2)$, which is about $2.5(\omega/c)$. From Eq. (44) we see that, when the heating function is a Gaussian, $\hat{H}_r(k_r)$ falls to 1% of its peak value when $(k_r\sigma)^2 = -4\ln(0.01)$ or $k_r = 4.3/\sigma$. So, if $4.3/\sigma < 2.5(\omega/c)$, or $\sigma > 1.7(c/\omega)$, then this sampling criterion will be sufficient. For a top hat source, Eq. (46) shows that $\hat{H}_r(k_r)$ is an oscillating function which falls to about 1% of its peak value when $k_r\sigma \approx 30$ and the criterion is $\sigma > 12(c/\omega)$.

As well as sampling sufficiently often to approximate accurately a rapidly oscillating integrand, it is necessary to sample sufficiently often to approximate spikes in the integrand. Undersampling a spike leads to aliasing or wraparound error in the transform domain. The wraparound error arising from $\hat{H}_z(\zeta)$ in Eq. (42) will be reduced by 60 dB if[11] the following conditions for the propagating and evanescent parts are met:

$$\Delta\phi < \frac{\mu\pi\log_{10}(e)}{3k}, \quad \Delta\phi < \frac{\mu\pi\log_{10}(e)}{3k\cosh\phi_{\max}}. \tag{49}$$

The ω integrals, Fourier transforms, that transform into the time domain must also be appropriately sampled. The criteria are that

$$\Delta\omega < \frac{\pi c}{r+z+\sigma}, \tag{50}$$

for the propagating part and

$$\Delta\omega < \frac{\pi c}{r\cosh\phi_{\max} + z\sinh\phi_{\max} + \sigma\cosh\phi_{\max}}, \tag{51}$$

for the evanescent part. The equivalent requirements to Eqs. (49) for the propagating and evanescent parts, respectively, are

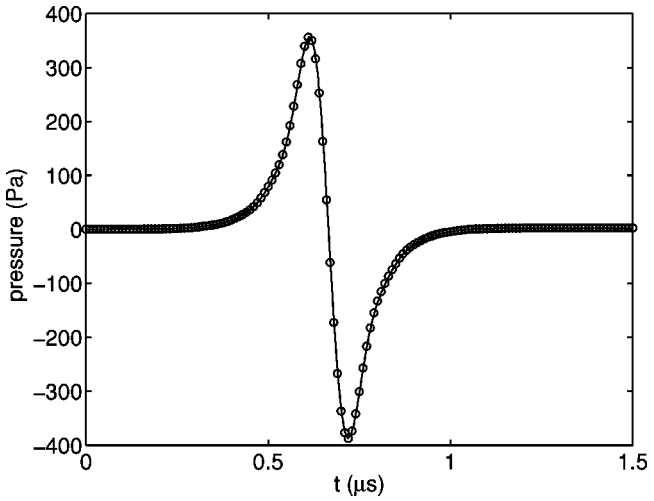

FIG. 2. Pressure 1 mm off axis and 1 mm below a pressure release boundary for an impulsive heating function with Gaussian radial profile. Model I (circles), model II (solid line). $\mu_a = 100\,\mathrm{cm}^{-1}$, $\sigma = 2$ mm, $V = -1$, $E_0 = 26\,\mu$J.

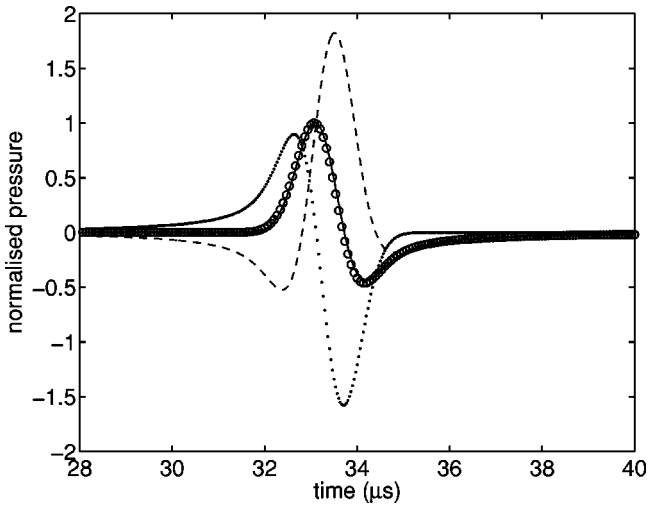

FIG. 3. Pressure 5 cm off axis for an infinitely long impulsive heating function with Gaussian radial profile. Diebold's analytic solution (circles), model II (solid) with the propagating (dashed), and evanescent (dotted) components also shown separately. $\mu_a = 0.01\,\mathrm{cm}^{-1}$, $\sigma = 1$ mm, $V = 1$.

$$\Delta\omega < \frac{\mu\pi c \log_{10}(\mathrm{e})}{3}, \quad \Delta\omega < \frac{\mu\pi c \log_{10}(\mathrm{e})}{3 \sinh \phi_{\max}}. \tag{52}$$

VI. TESTING THE MODELS

A. Time series calculations

Both models I and II can be used to calculate the time evolution of the pressure at a point, or at a receiver, due to an initial distribution $p_0(\mathbf{x})$. However, for signals containing high frequencies the mesh required for model I is large and the calculations are therefore slow. Model II, on the other hand, which calculates the pressure for many times at once, is better suited to time series calculation. Here, both models are compared to an analytical solution and to another model, described in the literature, that is based on a time-domain solution to the wave equation.

First, a simple test. Acoustic waves generated as described in Sec. II have the property that

$$\int_0^\infty p(t)\,\mathrm{d}t = 0. \tag{53}$$

This can be seen by considering the time integral of Eq. (8) with the Green's function given by Eq. (6). As the derivative of the delta function has the property $\int f(t)\delta'(t-t_0)\mathrm{d}t = -f'(t_0)$, and as the initial pressure distribution $p_0(\mathbf{x})$ is not a function of t, the time integral is zero. The time series generated by these numerical models were found to satisfy this property down to the machine precision.

To show that models I and II give the same pressure waveforms, the following example is calculated using both the cylindrically symmetric model II and model I (128^3 grid). The pressure at a point 1 mm off axis and 1 mm below a pressure-release acoustic boundary is shown in Fig. 2 for a Gaussian source [Eq. (43) with $\sigma = 2$ mm and $r = 1$ mm, and Eq. (41) with $\mu_a = 100\,\mathrm{cm}^{-1}$, $z_0 = 1$ mm, and $V = -1$]. The total energy in the pulse E_0 was 26 μJ. The circles show the pressure calculated using the 3D model I, and the solid line model II. Frequencies up to 5 MHz were included in the calculations. Clearly there is a good correspondence. As it is time consuming to calculate time series using model I, the remaining times series in this section are calculated using the cylindrically symmetric implementation of model II.

Diebold and Sun[4] present a solution to Eq. (1) for an infinitely long, cylindrical source with a Gaussian radial (beam) profile. We approximate such a source by setting $\mu_a = 0.01\,\mathrm{cm}^{-1}$ and $V = 1$ in Eq. (41). Frequencies up to 1 MHz were included. A comparison between Diebold's solution and model II for a point 5 cm off the source axis is given in Fig. 3. Diebold's solution is shown with circles. Model II (solid line) and its propagating (dashed) and evanescent (dotted) components are also shown. It is clear that in this case both the propagating and evanescent parts are required to describe the field correctly. The slight disagreement between the two (solid curve and circles) around 35 μs was due to the approximation of the infinite source by one that decays slowly ($\mu_a > 0$). It was necessary to make μ_a slightly larger than zero in order to satisfy the sampling conditions.

Poisson's solution to the wave equation[10] can be derived from Eqs. (6) and (8) and calculates a solution by summing over spherical surfaces S of radius $|\mathbf{x}-\mathbf{x}'| = ct$

$$p(\mathbf{x},t) = \frac{1}{4\pi c}\frac{\partial}{\partial t}\int_S \frac{p_0(\mathbf{x}')}{|\mathbf{x}-\mathbf{x}'|}\,\mathrm{d}S. \tag{54}$$

This time-domain model implicitly includes both propagating and evanescent components but is slow as it is not designed to use FFTs. Frenz *et al.*[8] use this model to calculate the acoustic field generated by the absorption of a pulse of light from an optical fiber by assuming the light generates a top hat heating function given by $H(z)$ in Eq. (41), with $\mu_a = 900\,\mathrm{cm}^{-1}$, $V = 1$, and $H(r)$ given by Eq. (45), with $\sigma = 300$ μm. (Actually they taper the edges of the beam profile slightly. We ignore this refinement for the sake of simplicity.) Time series were generated using these parameters with an implementation of the Poisson model described by Köstli and Beard[9] as well as with model II. The frequency response of both models was rolled off at high frequencies

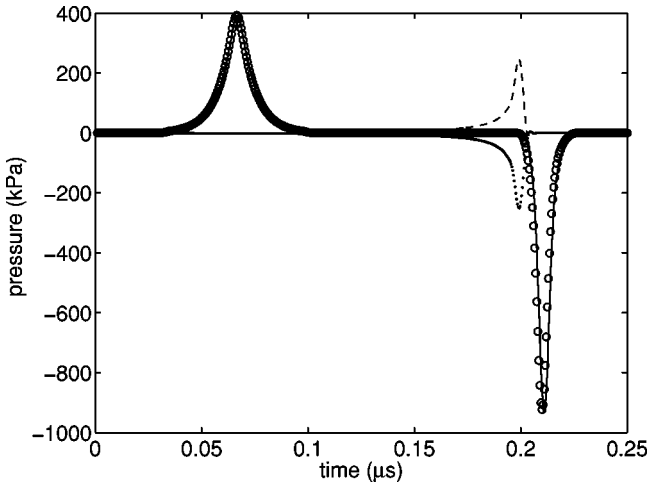

FIG. 4. Pressure on axis and 0.1 mm below the tip of an optic fiber (top hat profile) following impulsive heating calculated using Poisson model (circles) and model II (solid) with the propagating (dashed) and evanescent (dotted) components shown. $\mu_a = 900\ \mathrm{cm}^{-1}$, $\sigma = 300\ \mu\mathrm{m}$, $V = 1$, $E_0 = 26\ \mu\mathrm{J}$.

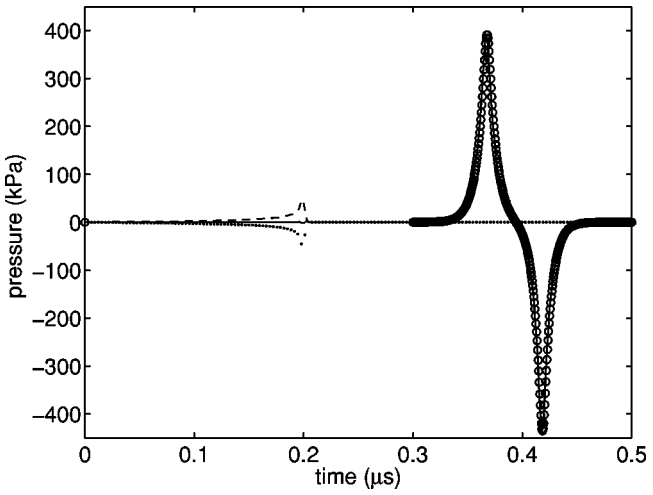

FIG. 6. Pressure on axis 0.55 mm below the tip of an optic fiber (top hat profile) following impulsive heating calculated using Poisson model (circles) and model II (solid) with the propagating (dashed) and evanescent (dotted) components shown. $\mu_a = 900\ \mathrm{cm}^{-1}$, $\sigma = 300\ \mu\mathrm{m}$, $V = 1$, $E_0 = 26\ \mu\mathrm{J}$.

(−3-dB point at 100 MHz). Figures 4–7 show the time series on axis at depths of 0.1 and 6.5 mm below the tip of the fiber, and at a depth of 0.55 mm both on axis and 0.3 mm off axis. The result from the Poisson model is shown as black circles, the total field from model II as a solid line, the propagating part of the field is a dashed line, and the evanescent part a dotted line. [These figures correspond to Figs. 3(a) and (b) in Frenz *et al.*]

In calculating the examples in Figs. 4 and 6, where the detector is close to the source region, model II (cylindrical version) was over 50 times faster than the Poisson model. For examples where the detector is further from the source region, though, there may be an advantage in using the Poisson model in that it can calculate the pressure for a range of times not starting from zero. Model II, on the other hand, always calculates the time series from $t = 0$. For the example in Fig. 5, to calculate the whole time series from zero to 4.4 μs the Poisson model would take 70 times as long as model II, but to calculate the portion of the time series shown took only three times as long. (This takes into account the fact that only the propagating waves contribute to the acoustic pressure in the far field, and it was therefore unnecessary to calculate the evanescent part, thereby decreasing the calculation time for model II at long distances.)

In the cylindrical version of model II used here, the singularity at $\zeta = 0$ was removed using a change of variables and the solution is thus no longer written as a Hankel transform from k_r to r. The time series for each radial position r must be calculated separately. However, if an alternative means of removing the singularity were used (see Sec. IV E), then the pressure time series at many values of r could be calculated at once via one fast Hankel transform (or via FFTs in the Cartesian case). The Poisson model does not have this po-

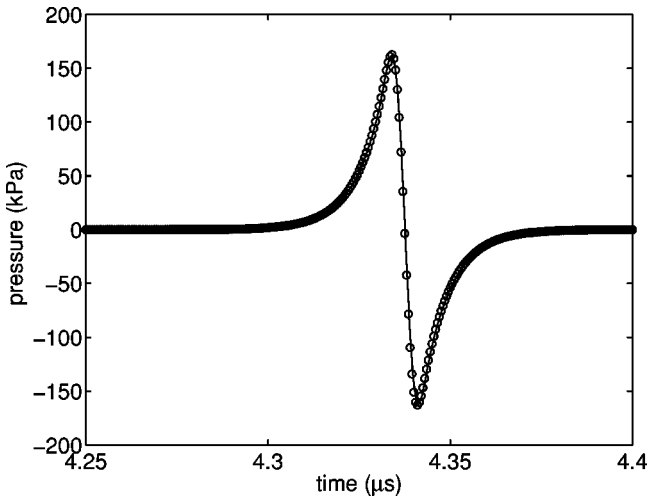

FIG. 5. Pressure on axis and 6.5 mm below the tip of an optic fiber (top hat profile) following impulsive heating calculated using Poisson model (circles) and model II (solid). The evanescent component is negligible. $\mu_a = 900\ \mathrm{cm}^{-1}$, $\sigma = 300\ \mu\mathrm{m}$, $V = 1$, $E_0 = 26\ \mu\mathrm{J}$.

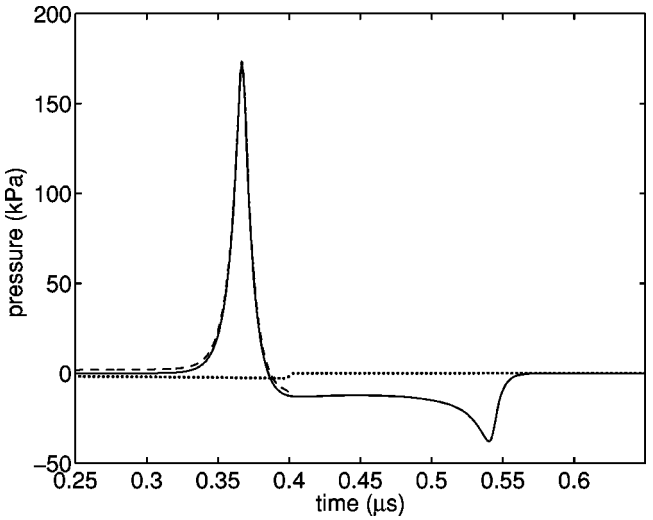

FIG. 7. Pressure 0.3 mm off axis and 0.55 mm below the tip of an optic fiber (top hat profile) following impulsive heating calculated using model II (solid) with the propagating (dashed) and evanescent (dotted) components shown. $\mu_a = 900\ \mathrm{cm}^{-1}$, $\sigma = 300\ \mu\mathrm{m}$, $V = 1$, $E_0 = 26\ \mu\mathrm{J}$.

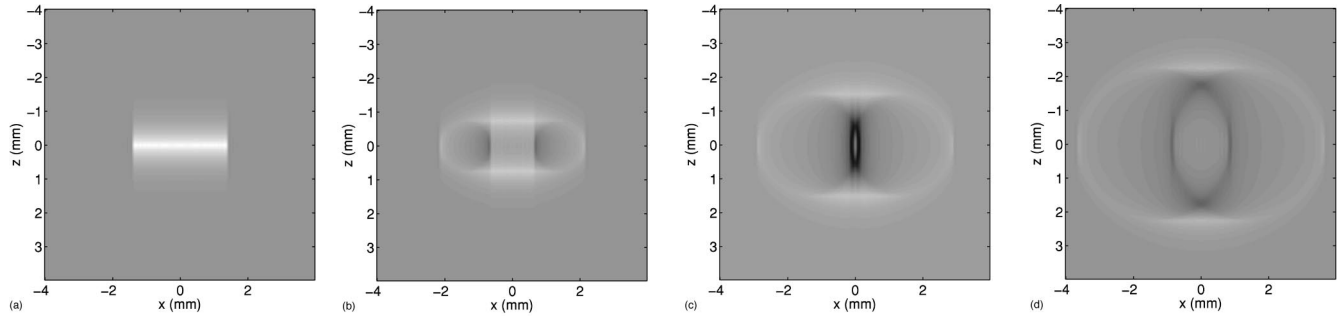

FIG. 8. 8×8 mm slices through an axis-symmetric 3D pressure field with a top hat initial pressure distribution. $\sigma=1.4$ mm, $\mu_a=25\ \mathrm{cm}^{-1}$, $V=1$ (reflecting boundary), $E_0=26\ \mu$J. From left to right, the four frames show the initial pressure distribution $p_0(\mathbf{x})$, then the pressure $p(\mathbf{x},t)$ at 0.5, 1, and 1.5 μs, respectively. The linear gray scale ranges from −1.6 kPa (black) to 1.2 kPa (white).

tential and is limited to calculating the pressure time series at one point. For the calculation of the signals arriving at a linear array of detectors, then, such an implementation of model II would be much more efficient for many practical situations.

B. Experimental validation

The comparisons above, between time series generated using the *k*-space models described here and both an analytical solution and a numerical time domain model, show that these *k*-space models correctly calculate solutions to Eq. (1). What they do not test are the assumptions made in deriving this equation (negligible heat conduction and viscosity, and linearity approximations). Experiments are required in order to test the applicability of Eq. (1) to photoacoustic generation in fluids. One challenge such experiments present is that, to ensure a fair comparison between model and experiment, it is necessary to know the frequency-dependent directional response of the ultrasound sensor, $\mathcal{D}$. This work is still progressing but initial experiments show good agreement between these models and such experiments.[29]

VII. OTHER APPLICATIONS OF THE MODELS

A. Model I: Visualization of the acoustic field

For calculating time series model I is slow, as the whole field is calculated at each instant of time. For visualizing the evolution of the whole field, though, it is ideally suited. The whole field can be viewed at any chosen time instant without the need to step forward in time, as is required in finite difference methods.

Figures 8–10 show examples of pressure fields calculated using model I. Each example shows 8×8-mm slices through an axis-symmetric 3D pressure field calculated on a 3D mesh of 128^3 points. (z and r both range from −4 to 4 mm.) In all of these examples the top half of the picture is there purely to enable calculation of the effect of a boundary on the acoustic field in the bottom half. The field that would be realized in practice, then, is just the bottom half. In Fig. 8 the initial pressure has a top hat profile in r and decays exponentially with $|z|$. In this case, the upper half of p_0 is an image source representing an acoustic reflection from a rigid boundary. An initial pressure distribution such as this, shown in the leftmost image, may be generated in practice by sending a laser pulse along a multimode fiber which terminates in a homogeneous optically absorbing liquid. The other three images are snapshots of the field at 0.5, 1.0, and 1.5 μs later. The negative pressure region that develops close to the rigid boundary—the dark area in the third picture—is due to the edge waves and shows clearly why cavitation has been observed in a case such as this. Indeed, Frenz *et al.* have photographed the cavitation and the edge waves generated in this way using Schlieren methods.[8,30]

Figure 9 is similar to Fig. 8 except that instead of modeling a solid–fluid interface at $z=0$ there is an acoustic pressure-release, air–fluid boundary. The reflection from this is represented by the negative (dark) region in the top half of the first image. This results in a large negative part to the bipolar signal, as the subsequent images show. Figure 10, in which the top hat profile is replaced with a Gaussian, shows that by removing the sharp radial discontinuity, the edge

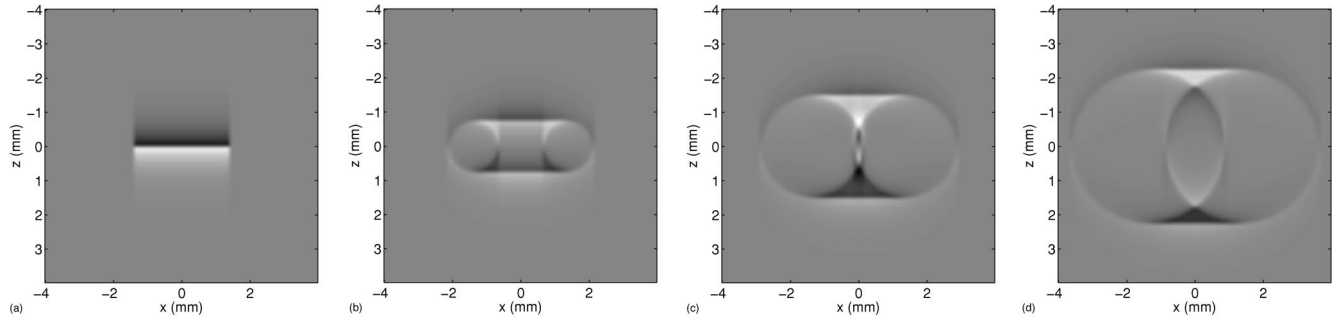

FIG. 9. Tophat laser pulse incident on an absorbing fluid at a pressure-release boundary. As Fig. 8 except $V=-1$. The frames show the pressure distribution $p(\mathbf{x},t)$ at $t=0$, 0.5, 1, and 1.5 μs, respectively. Gray scale range: −1.1 kPa (black) to 1.1 kPa (white).

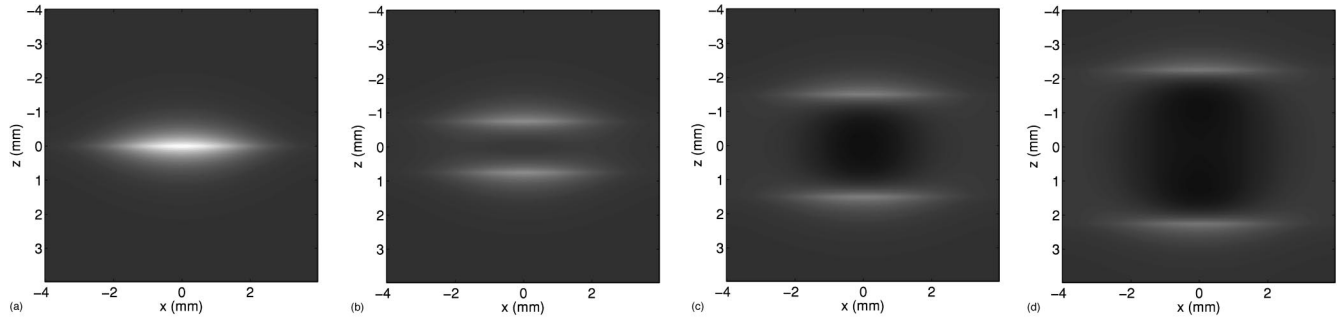

FIG. 10. As Fig. 8 except $H_r(r)$ has a Gaussian rather than a top hat profile (1/e point at $r=2$ mm). Edge waves are not generated. The frames show the pressure distribution $p(\mathbf{x},t)$ at $t=0$, 0.5, 1, and 1.5 μs, respectively. Gray scale range: -87 Pa (black) to 550 Pa (white).

waves are less distinct, and the field does not develop such a large negative pressure.

B. Model II: Simulation of array measurements

As we have seen above, model II can be used to generate photoacoustic time series efficiently. Figure 11 shows a simulation of time series measured along a linear array in response to photoacoustic point sources 1.5 and 3 mm above the detector plane. The time series are placed side by side and the linear gray scale indicates the acoustic pressure. (The white and black ends of the gray scale indicate positive and negative acoustic pressures, respectively.)

Acoustic array measurements are used in many applications including photoacoustic imaging,[21] in which the aim is to estimate the initial pressure distribution $p_0(\mathbf{x})$ from a set of time series measurements obtained over a line or plane. The models described here can be used to generate synthetic, noise-free, time series data in order to test aspects of such problems. For instance, the time series in Fig. 11 could represent the acoustic signals recorded by a line array of detectors perpendicular to two blood vessels which have been illuminated with a laser pulse. These data could be used to test photoacoustic image reconstruction algorithms.

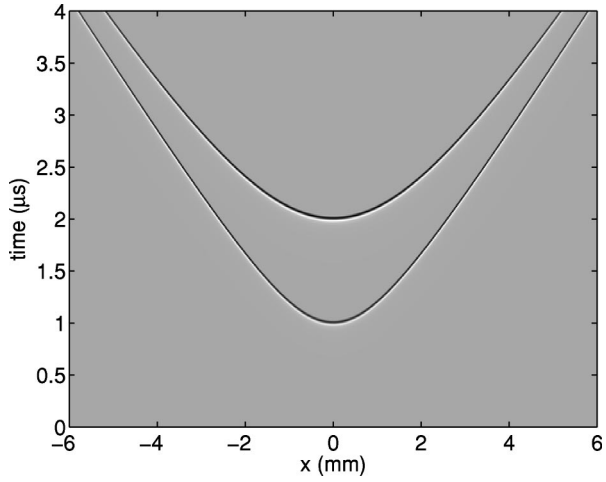

FIG. 11. Simulation of time series measured along a line array of detectors with two point photoacoustic sources at depths of 1.5 and 3 mm. The linear gray scale is in arbitrary units ranging from negative (black) to positive (white) pressures.

C. Model II: Radiation patterns

The emphasis in this paper is on the ability of model II to generate time series efficiently. However, as well as calculating time series, model II can be used to generate single-frequency or broadband radiation patterns of photoacoustic sources. The (complex) pressure at a single frequency may be calculated using Eqs. (26) and (32), without the final Fourier transform in time, or Eqs. (37) and (38). As above, the propagating and evanescent parts of the radiating field may be computed separately. Radiation patterns generated in this way are shown in Cox *et al.*[29]

In addition, because the velocity potential ψ is related to the complex pressure by $\psi=p/(i\omega\rho)$, model II can be simply adapted to calculate it. The complex particle velocity $\mathbf{v}$ and acoustic intensity $\mathbf{I}$ then follow using the standard relations: $\mathbf{v}=\nabla\psi$ and $\mathbf{I}=p\mathbf{v}$. In this way, model II can be used to calculate single-frequency and broadband intensity plots.

VIII. SUMMARY

Two related numerical models for calculating the acoustic field in a fluid following the absorption of a pulse of light have been described. Model I uses an exact time propagator to calculate the acoustic field at all points on a spatial grid for one moment of time in a single step. It can be used to visualize the 3D evolution of a photoacoustically generated wave field through time. Model II calculates pressure time series for points on a line or plane by mapping from the vertical spatial wavenumber to temporal frequency. The use of this mapping, and an FFT to perform part of the calculation, makes this an efficient model. As it calculates the propagating and evanescent parts of the field separately, model II can also be used to calculate the near- and far-field radiation patterns of photoacoustic sources and, with one small change, can be used to calculate velocity potential and thus particle velocity and acoustic intensity vectors. The effect on the measured pressure of a finite-sized planar detector with arbitrary frequency-dependent directional response can be included simply in either model—a necessary requirement when simulating measurements made with real detectors. Time series from both of these *k*-space models were tested against an analytical solution and a well understood but slower numerical model based on Poisson's solution to the wave equation.

ACKNOWLEDGMENTS

The authors are grateful to Kornel Köstli for programming the Poisson model used in Sec. VI A. This work has been supported by the Engineering and Physical Sciences Research Council, UK.

[1] A. C. Tam, "Applications of photoacoustic sensing techniques," Rev. Mod. Phys. **58**(2), 381–431 (1986).
[2] G. J. Diebold and P. J. Westervelt, "The photoacoustic effect generated by a spherical droplet in a fluid," J. Acoust. Soc. Am. **84**(6), 2245–2251 (1988).
[3] G. J. Diebold, T. Sun, and M. I. Khan, "Photoacoustic monopole radiation in 1-dimension, 2-dimension, and 3-dimension," Phys. Rev. Lett. **67**(24), 3384–3387 (1991).
[4] G. J. Diebold and T. Sun, "Properties of photoacoustic waves in one-dimension, 2-dimension, and 3-dimension," Acustica **80**(4), 339–351 (1994).
[5] M. I. Khan and G. J. Diebold, "The photoacoustic effect generated by an isotropic solid sphere," Ultrasonics **33**(4), 265–269 (1995).
[6] M. I. Khan and G. J. Diebold, "The photoacoustic effect generated by laser irradiation of an isotropic solid cylinder," Ultrasonics **34**(1), 19–24 (1996).
[7] G. Paltauf, H. SchmidtKloiber, and H. Guss, "Light distribution measurements in absorbing materials by optical detection of laser-induced stress waves," Appl. Phys. Lett. **69**(11), 1526–1528 (1996).
[8] M. Frenz, G. Paltauf, and H. SchmidtKloiber, "Laser-generated cavitation in absorbing liquid induced by acoustic diffraction," Phys. Rev. Lett. **76**(19), 3546–3549 (1996).
[9] K. Köstli and P. Beard, "Two-dimensional photoacoustic imaging by use of Fourier-transform image reconstruction and a detector with an anisotropic response," Appl. Opt. **42**(10), 1899–1908 (2003).
[10] L. Landau and E. Lifshitz, *Fluid Mechanics*, 2nd ed. (Butterworth Heinemann, Oxford, 1987).
[11] F. Jensen, W. Kuperman, M. Porter, and H. Schmidt, *Computational Ocean Acoustics* (Springer, New York, 2000).
[12] X. Wang, Y. Pang, G. Ku, X. Xie, G. Stoica, and L. V. Wang, "Noninvasive laser-induced photoacoustic tomography for structural and functional *in vivo* imaging of the brain," Nat. Biotechnol. **21**(7), 803–806 (2003).
[13] X. Wang, Y. Pang, G. Ku, G. Stoica, and L. V. Wang, "Three-dimensional laser-induced photoacoustic tomography of mouse brain with the skin and skull intact," Opt. Lett. **28**(19), 1739–1741 (2003).
[14] C. G. A. Hoelen, F. F. M. de Mul, R. Pongers, and A. Dekker, "Three-dimensional photoacoustic imaging of blood vessels in tissue," Opt. Lett. **23**(8), 648–650 (1998).
[15] P. C. Beard, "Photoacoustic imaging of blood vessel equivalent phantoms," Proc. SPIE **4618**, 54–62 (2002).
[16] G. Paltauf and P. E. Dyer, "Photomechanical processes and effects in ablation," Chem. Rev. (Washington, D.C.) **103**(2), 487–518 (2003).
[17] If the pulse is too long for stress confinement but short enough for thermal confinement then, if we can separate the heating function into $\mathcal{H}(\mathbf{x},t) = H(\mathbf{x})H_t(t)$, where $H_t(t)$ describes the temporal shape of the pulse, the pressure due to a longer pulse may be written as the convolution $\int p(t - t')H_t(t')\mathrm{d}t'$, where $p(t)$ is the pressure due to δ function heating. Note that a moving source is not separable into spatial and temporal parts, and so cannot be modeled using the methods described in this paper, unless the source is moving much more slowly than the speed of sound and may be approximated as stationary.
[18] J. D. Jackson, *Classical Electrodynamics* (Wiley, New York, 1962), pp. 183–187.
[19] A. J. Healey, S. Leeman, and J. Weight, "Space-time imaging of transient ultrasound fields," Int. J. Imaging Syst. Technol. **8**, 45–51 (1997).
[20] M. S. Howe, *Acoustics of Fluid-Structure Interactions* (Cambridge University Press, Cambridge, 1998), p. 38.
[21] K. P. Köstli, M. Frenz, H. Bebie, and H. P. Weber, "Temporal backward projection of optoacoustic pressure transients using Fourier transform methods," Phys. Med. Biol. **46**(7), 1863–1872 (2001).
[22] D. R. Bacon, "Characteristics of a PVDF membrane hydrophone for use in the range 1–100 MHz," IEEE Trans. Sonics Ultrason. **SU-29**, 18–25 (1982).
[23] P. C. Beard, F. Perennes, and T. N. Mills, "Transduction mechanisms of the Fabry–Perot polymer film sensing concept for wideband ultrasound detection," IEEE Trans. Ultrason. Ferroelectr. Freq. Control **46**(6), 1575–1582 (1999).
[24] M. J. S. Lowe, "Matrix techniques for modeling ultrasonic waves in multilayered media," IEEE Trans. Ultrason. Ferroelectr. Freq. Control **42**(4), 525–542 (1995).
[25] B. W. Suter and R. A. Hedges, "Understanding fast Hankel transforms," J. Opt. Soc. Am. A **18**, 717–720 (2001).
[26] M. J. Cree and P. J. Bones, "Algorithms to numerically evaluate the Hankel transform," Comput. Math. Appl. **26**, 1–12 (1993).
[27] M. Born and E. Wolf, *Principles of Optics: Electromagnetic Theory of Propagation, Interference and Diffraction of Light*, 7th ed. (Cambridge University Press, Cambridge, 1999).
[28] L. C. Andrews and B. K. Shivamoggi, *Integral Transforms for Engineers and Applied Mathematicians* (Macmillan, New York, 1987).
[29] B. T. Cox, J. Laufer, K. Köstli, and P. Beard, "Experimental validation of photoacoustic *k*-space propagation models," Proc. SPIE **5320**, 238–248 (2004).
[30] G. Paltauf, H. Schmidt-Kloiber, and M. Frenz, "Photoacoustic waves excited in liquids by fiber-transmitted laser pulses," J. Acoust. Soc. Am. **104**(2), 890–897 (1998).